Biosensors and Bioelectronics 141 (2019) 111470

Contents lists available at ScienceDirect

Biosensors and Bioelectronics

journal homepage: www.elsevier.com/locate/bios

Integrating polythiophene derivates to PCN-222(Fe) for electrocatalytic sensing of L-dopa

Yuling Chen, Xin Sun, Sudip Biswas, Yao Xie, Yang Wang*, Xiaoya Hu**

School of Chemistry and Chemical Engineering, Yangzhou University, Yangzhou, 225002, China

ARTICLE INFO

Keywords:
Porphyrinic metal-organic frameworks
Poly(3-methythiophene)
Chemical polymerization
Levodopa detection

ABSTRACT

Porphyrinic Metal-Organic Frameworks (porph-MOFs) are attracting attention due to the redox activity in the porphyrin subunit. Herein, we report the design of a novel core-shell structure hybrid material with a sea-cucumber morphology, namely PMeTh, containing the poly(3-methythiophene) conducting polymer coated on the surface of iron-based porph-MOFs PCN-222(Fe) via in-situ oxidative chemical polymerization. The porous PCN-222(Fe) serves as the electrocatalytic sites, while the poly(3-methythiophene) conducting polymer functions as the charge collector to facilitate the charge transport to the redox active sites. The resulting PMeTh composite demonstrates an excellent electrochemical response towards the levodopa detection. The sensitivity towards the L-dopa detection is estimated to be 1.868 μA · μM^{-1} · cm^{-2} in the linear concentration of 0.05–7.0 μmol · L^{-1} and 0.778 μA · μM^{-1} · cm^{-2} in the linear concentration of 7.00–100 μmol · L^{-1}, respectively. Additionally, the levodopa sensor exhibits a low detection limit of 2 nmol L^{-1} as well as excellent stability after 120 cycles in 10 μmol L^{-1} levodopa. The feasibility of this novel L-dopa sensor was evaluated in human urine samples by standard addition. The satisfactory recoveries were in the range of 97.0–104.5% with the R.S.D. value lower than 4.4%. The method of intergrating porph-MOFs and conducting polymers can efficiently expand the porph-MOFs based composites in bioanalysis.

1. Introduction

Parkinson's disease (PD) is the well-known neurodegenerative disease caused from the depletion of dopamine (DA) in their brains. As the precursor of the DA, levodopa (3,4-dihydroxy-L-phenylalanine, L-dopa) is capable to cross the blood-brain barrier into the central nervous system and has been recognized as the most efficient therapeutic drug for PD patients (Damier et al., 1999). However, epidemiological studies have revealed that the elevated levels of L-dopa for chronic use conversely can bring many other side effects (Thanvi and Lo, 2004). Analytical techniques have been proposed for L-dopa detection including high performance liquid chromatography (HPLC) (Soumyanath et al., 2018), fluorescence (Liu and Zhu, 2019), capillary zone electrophoresis (Zhang et al., 2001), and electrochemical sensor (Shahrokhian and Asadian, 2009). In comparison with other methods, electrochemical methods offer the advantages of low cost, high sensitivity, easy operation and time-saving for the determination of L-dopa.

Metal-organic frameworks (MOFs) are one type of three-dimensional (3 D) porous materials that are constructed from the organic linkers and metal or metal-cluster connecting nodes (Liang et al., 2018). Due to the versatility of MOFs, such as extra-large surface area, structural adaptivity and flexibility, ordered crystalline pores, and abundant coordination sites, MOFs have been widely applied in diverse fields including gas adsorption and separation (Zhang et al., 2017), catalysis (Sheng et al., 2018), and chemical sensing (Kreno et al., 2012). In addition, these features also make attractive for MOFs to be a potential candidate for electrocatalysis and sensing. However, by comparison with other research fields aforementioned, the MOFs utilized as the electrocatalysis was a relatively new field (Chen et al., 2018; Wang et al., 2016a, 2016b; Kung et al., 2015).

As a subclass of MOFs, porphyrinic MOFs (porph-MOFs) have gained burgeoning attention in various electrocatalytic applications because of their redox activity in porphyrin subunits (Wu et al., 2017; Ma et al., 2010). However, the semi-conductivity behavior of porphyrins limits their further applications. At this time, integrating porph-MOFs into a conducting polymer have been recognized as an efficient method to enhance the electroconductivity (Wang et al., 2017; Sun et al., 2014). Inspired by the above work, a novel electrochemical sensor was successfully prepared by polymerizing the conductive polymer around the MOFs. Poly(3-methythiophene) (P3MT) is selected

* Corresponding author.
** Corresponding author.
E-mail addresses: wangyzu@126.com (Y. Wang), xyhu@yzu.edu.cn (X. Hu).

https://doi.org/10.1016/j.bios.2019.111470
Received 14 June 2019; Accepted 22 June 2019
Available online 25 June 2019

as the charge collector to facilitate the mass transport. PCN-222(Fe), a typical metalloporphyrin MOF, is selected as a host material to support the in-situ oxidative chemical polymerization of P3MT, owing to its ultrahigh surface area and excellent chemical stability (Wang et al., 2018). The P3MT polymer is spontaneously grown on the surface of the PCN-222(Fe) under the oxidant of $FeCl_3$ and the core-shell PMeTh composites are finally prepared. The composites function as the electrode materials are found sensitive and selective to the L-dopa molecules. The feasibility of the PMeTh-based sensor is applied in the human urine samples for L-dopa detection and satisfactory has obtained in our work.

2. Experimental section

2.1. Synthesis of PCN-222(Fe)

The Fe-TCPP ligand was synthesized as the procedure in the supporting information (Feng et al., 2012). The synthetic procedure of PCN-222(Fe) was modified based on a published protocol (Li et al., 2015). $ZrOCl_2 \cdot 8H_2O$ (50 mg) and C_6H_5COOH (0.75 g) in 10 mL DMF were absolutely dissolved in a 20 mL Pyrex vial under ultrasonication. The obtained colorless solution was then heated in an oven at 80 °C for 1 h. After cooling down to the room temperature, 25 mg Fe-TCPP was ultrasonically dissolved for 5 min. The dark brown suspension was placed in an oven at 120 °C for 1 h. After cooling down to the room temperature, the mixture was isolated by centrifugation, washed with DMF and dipped in acetone for 24 h by three repeated cycles. The dark brown microcrystalline powder was eventually obtained after it was dried in a vacuum at 120 °C for 24 h.

2.2. Activation of PCN-222(Fe)

50 mg of PCN-222(Fe) was dissolved in 20 mL DMF and 4 mL HCl (8 mol L^{-1}) and the mixture was reacted in an oven at 100 °C for 24 h. After cooling down to the room temperature, the dark brown needle shaped crystals was isolated by centrifugation and dipped twice in the acetone for 12 h. The activated PCN-222(Fe) was harvested after drying in the vacuum at 120 °C for 12 h.

2.3. Synthesis of PCN-222(Fe)/poly(3-methythiophene) (PMeTh)

For the synthesis of PMeTh (Fig. 1A), the in-situ chemical oxidative polymerization method was used in this work. Firstly, 10 mg PCN-222(Fe) was dispersed in 5 mL $CHCl_3$ under ultrasonic vibrations at room temperature for 1 h. Then, 500 µL 3 MT monomer was added in the above solution and stirred at room temperature for 4 h. In another beaker, 0.2 g $FeCl_3$ was absolutely dissolved in 20 mL $CHCl_3$ under ultrasonication for 1 h. Secondly, the well-dispersed solution of PCN-222(Fe) and 3 MT monomer was slowly and dropwise added to the $FeCl_3$ solution. The mixture was vigorously stirred at room temperature for 24 h. The resultant powder was harvested by centrifugation and washed three times with methanol, distilled water and acetone by turns. The black powder was finally collected after vacuum-dried at 60 °C for 12 h. The P3MT was prepared in the same way but without the addition of 10 mg PCN-222(Fe) in the solution of 3 MT monomer and $CHCl_3$.

2.4. Preparation of PMeTh/GCE

Prior to each electrochemical experiment, the bare GCE was polished with 0.3 µm and 0.05 µm α-Al_2O_3 slurries on chamois leather successively. After that, the polished GCE was sonicated with ethanol and distilled water for 2 min to obtain a mirror-like surface. 1 mg PMeTh composite was absolutely dissolved in the 1 mL water under ultrasonication for 5 min. Then 5 µL of 1 mg mL^{-1} PMeTh water solution was dropped on the surface of GCE and dried in a desiccator. Two hours later, 2 µL of 5% chitosan solution was casted on the PMeTh layer and dried for another 2 h. For comparison, P3MT/GCE, PCN-222(Fe)/GCE, and bare GCE were also fabricated in the similar way.

3. Results and discussion

3.1. Structural characterization of materials

The crystalline structure and phase purities of PMeTh composite were primarily characterized by XRD. As displayed in Fig. 2A, the main characteristic diffraction peaks at 4.65, 6.88, 8.03 and 9.45 degrees of PCN-222(Fe) matches well with those reported in the literature (Li et al., 2017), indicating the PCN-222(Fe) was synthesized successfully. The values are in agreement with the (2 2 0), (2 0 1), (3 –1 1) and (4 0

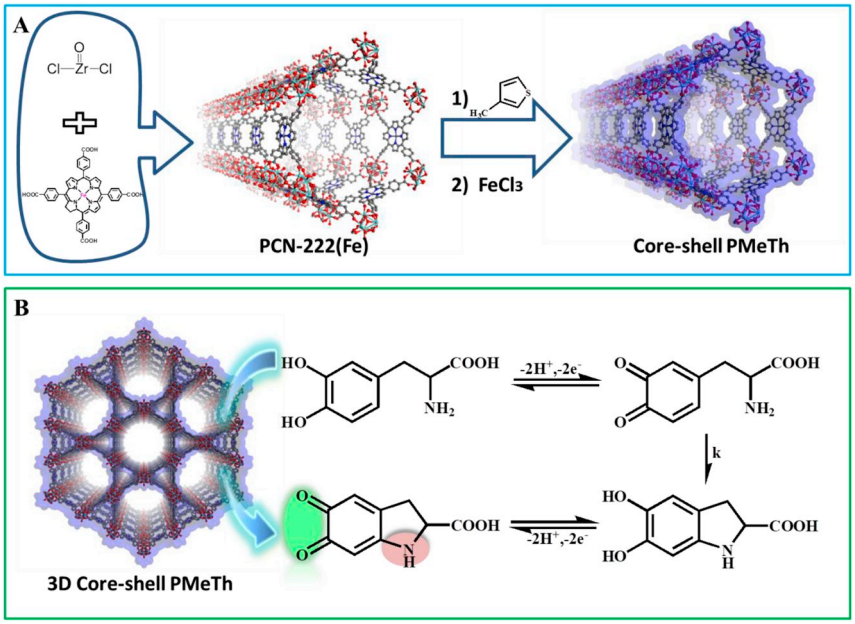

Fig. 1. Schematics of the preparation of PMeTh (A) and the proposed mechanism of L-dopa oxidation at the PMeTh/GCE (B).

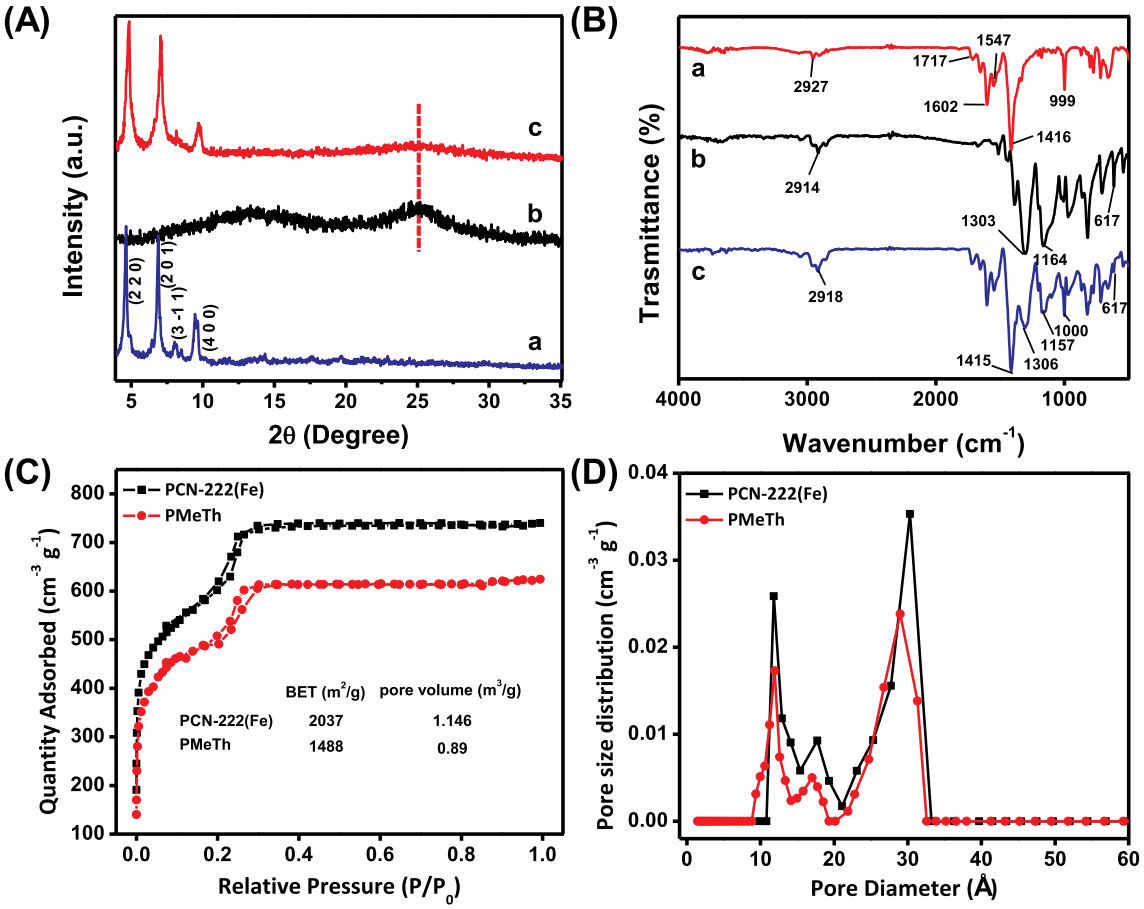

Fig. 2. (A) XRD patterns and (B) FTIR patterns of pure PCN-222(Fe) (a), P3MT (b), and PMeTh (c). (C) The nitrogen sorption isotherms of PCN-222(Fe) and PMeTh at 77 K up to 1 bar. (D) DFT pore size distribution of PCN-222(Fe) and PMeTh.

0) panels as observed in Fig. 2A. Only board peaks at around 13° and 25° are observed in the XRD pattern of P3MT, which probably due to the amorphous structure of this π conjugated polymer (Han et al., 2015). After the P3MT polymer was spontaneously grown on the surface of PCN-222(Fe), it can be seen that only a weak characteristic peak for non-crystalline P3MT was found in the XRD image. The results signify that the successful preparation of PMeTh composite without impurities. In addition, from the preserved diffraction peaks of PCN-222(Fe), it can be speculated that the in-situ oxidative chemical polymerization of 3 MT won't destroy the crystalline of PCN-222(Fe).

The FTIR spectra (Fig. 2B) provided a direct proof that the preparation of PMeTh composite. For the pristine PCN-222(Fe) (curve a), the IR band at 1717 (w), 1602 (s), 1547 (s), 1416 (vs) cm^{-1} are the characteristics for the big ring skeleton absorptions. And the strong peak at 999 cm^{-1} is assigned to the Fe–N stretching vibration in the Fe-TCPP (Shi et al., 2018). Compared with PCN-222(Fe), the curve c of PMeTh shows the new peaks, including 1306 cm^{-1} for the deformation vibrations of methyl groups, 1157 cm^{-1} for the C–H ring breathing and the peaks at 617 cm^{-1} for the C–S–C stretching vibrations in the thiophene ring (Madani et al., 2015). These additional peaks are in good accordance with the IR band of P3MT (curve b), validating the formation of PMeTh composite.

The N_2 adsorption–desorption curves at 77 K and pore size distribution of PCN-222(Fe) and PMeTh are shown in Fig. 2C and D. A typical type IV isotherm for PCN-222(Fe) was observed, suggesting that PCN-222(Fe) is a porous material with micropores and mesopores. The Brunauer–Emmett–Teller (BET) data and the corresponding total pore volumes for PCN-222(Fe) and PMeTh are shown in Fig. 2C. The initial, activated PCN-222(Fe) isotherm shows a BET specific surface area of 2037 $m^2 g^{-1}$. After the P3MT coated on the surface of the PCN-222(Fe), the surface area of PMeTh composite was found to be 1488 $m^2 g^{-1}$. The loss of surface area after polymerization is mainly due to the location of P3MT inside the PCN-222(Fe) pores (Abraira et al., 2019). As displayed in Fig. 2D, the pore size distribution for PCN-222(Fe) and PMeTh was calculated on the basis of density functional theory (DFT) simulation. The PMeTh composite showed a similar pore size distribution, suggesting that the overall retention of the triangular microchannels and hexagonal mesochannels in PCN-222(Fe). Such high surface area with a typical porosity makes it possible for PMeTh composite to be an excellent electrode modifier.

The geometrical and morphological structures of the synthesized PMeTh composite were characterized by TEM and SEM. As shown in Fig. 3A and B, the morphology of PCN-222(Fe) is comparatively regular and exists as a typical rod-like structure with 1.45 μm in length. After growth of P3MT, as depicted in Fig. 3C, the rod-like structure of PCN-222(Fe) was retained but with an amorphous shell coated on its smooth surface. This finding suggests that the successful formation of core-shell PMeTh composite. The SEM image of PMeTh (Fig. 3D) exhibited a sea-cucumber like structure with a rough surface, which is in obvious contrast with the pristine rod-like PCN-222(Fe), consolidating the formation of core-shell PMeTh. Furthermore, with a view to observe the elemental distribution of PMeTh composite, the characterization was carried out on HAADF-STEM and the results were shown in Fig. 4. From the EDS-TEM mapping images of Fig. 4(c–i), it can be seen that all the elements for PMeTh are in homogenous and uniform distribution. In addition, the diameter for S element (Fig. 4i) is much longer than that of Zr (Fig. 4h), which is the important composition for PCN-222(Fe), indicating the P3MT conjugated polymer successfully coated on the surface of metalloporphyrin MOF. The results are completely conformed to that provided by SEM and TEM images (Fig. 3).

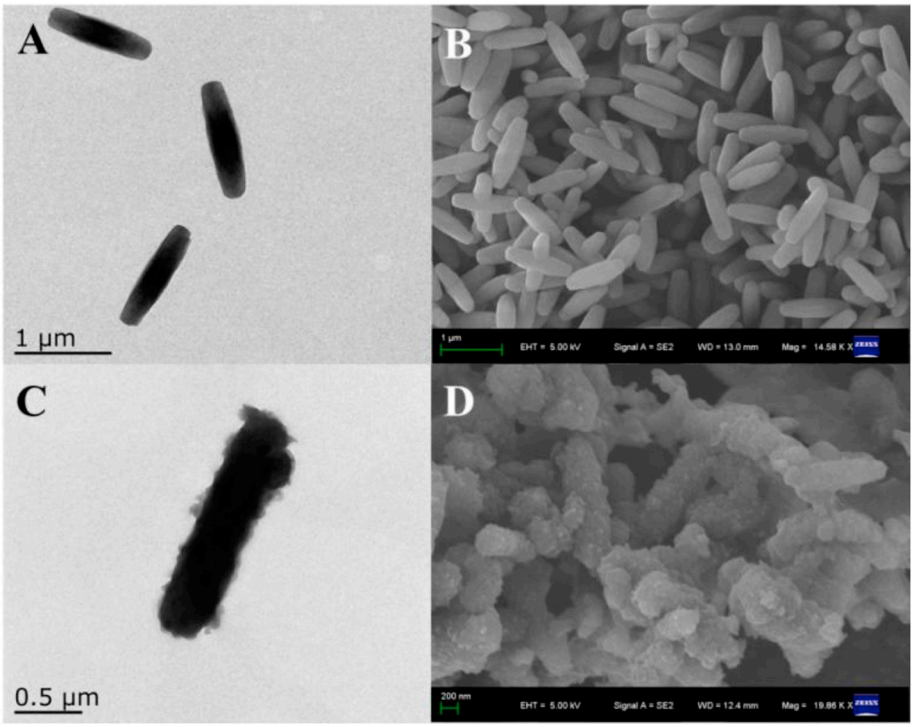

Fig. 3. TEM (A) and SEM (B) images of PCN-222(Fe). TEM (C) and SEM (D) images of PMeTh.

3.2. Electrochemical behavior of core-shell PMeTh composite

It is known that the electrochemical impedance spectroscopy (EIS) was a powerful tool to investigate the interface properties and changes in electrochemical properties of the surface-modified electrodes. A typical impedance spectrum usually consists of a semicircle part corresponding to the electron-transfer limited process and a linear part resulting from the diffusion process of electrons (Huang et al., 2010). As a representative of the electron transfer resistance (R_{ct}), the semicircle part is impacted by the dielectric and insulating features at the electrodel electrolyte interface. Fig. 5A shows the Nyquist plot of four different modified electrodes in the frequency of 0.1–10 kHz. It can be seen that the R_{ct} value of 208 Ω for bare GCE decreased to 120 Ω after the immobilization of redox-active PCN-222(Fe). With the same

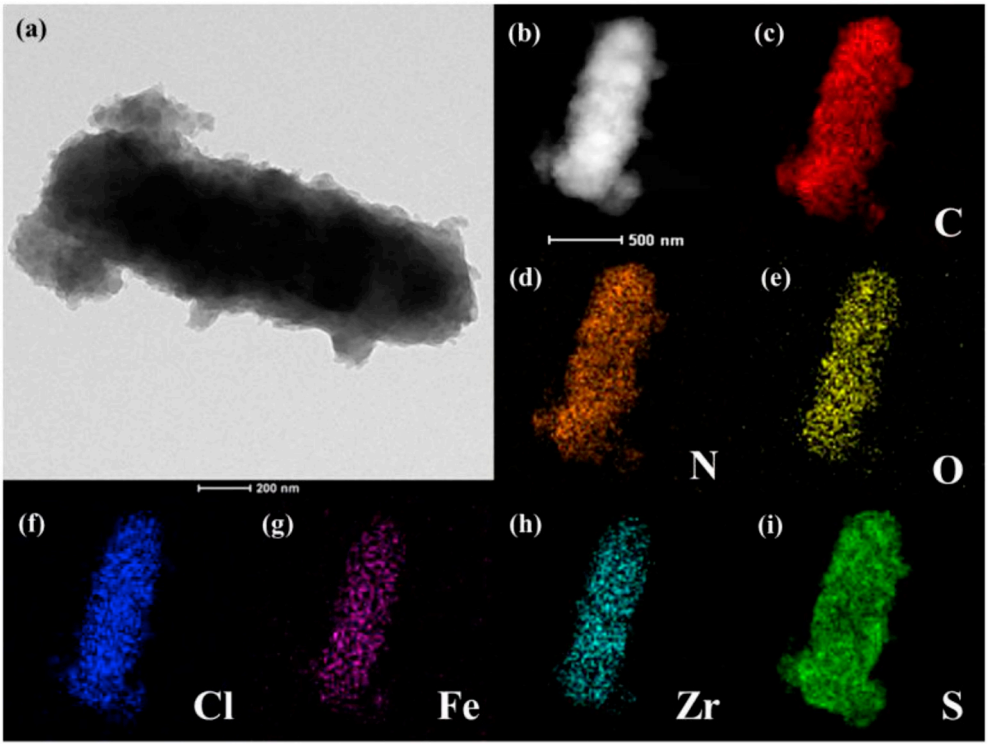

Fig. 4. Bright-field (a) and dark-field (b) in HAADF images of PMeTH composite. (c–i) EDS-TEM mapping images of PMeTH composite.

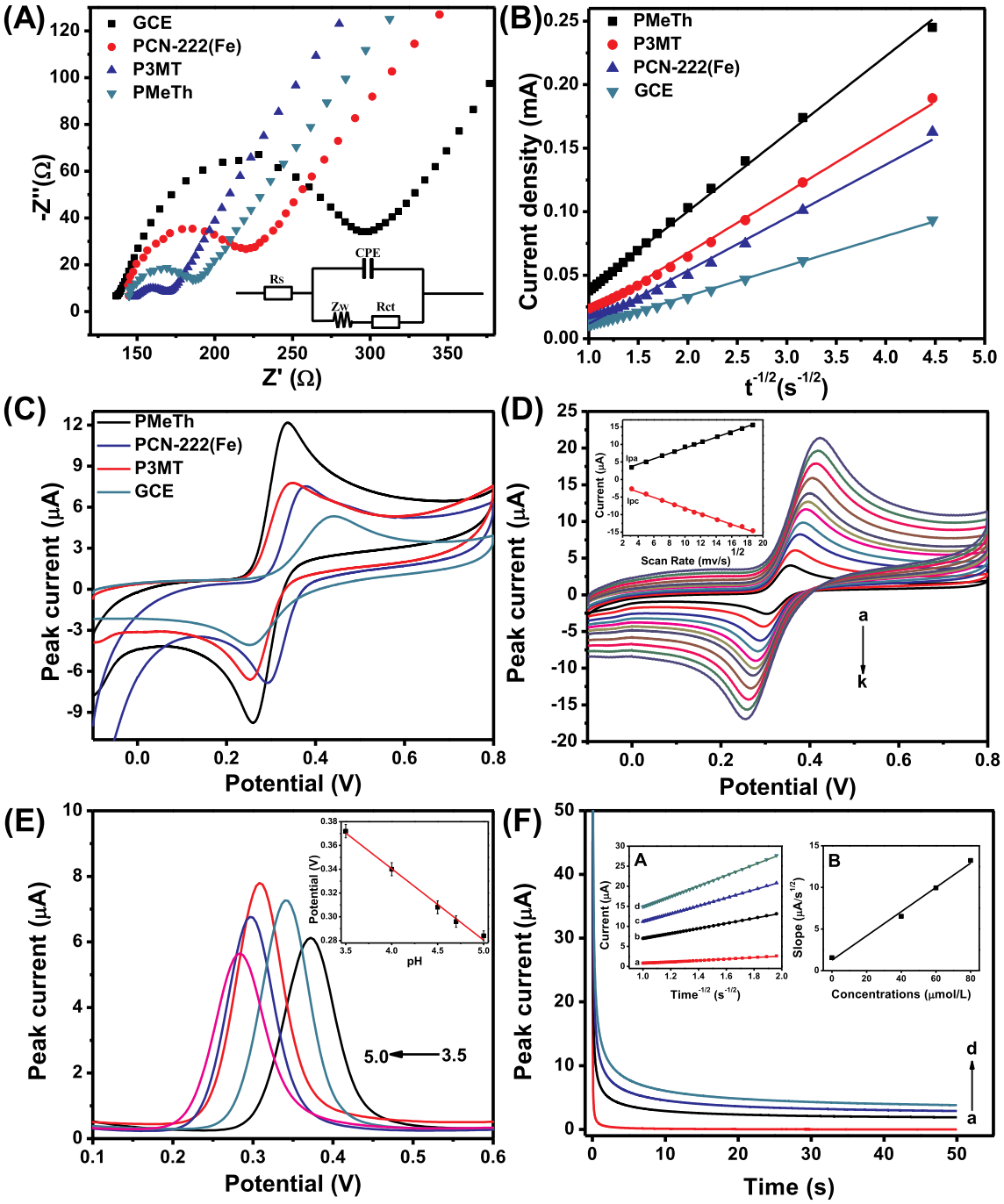

Fig. 5. (A) Electrochemical impedance spectroscopy of GCE, PCN-222(Fe)/GCE, P3MT/GCE and PMeTh/GCE in 5.0 mmol L^{-1} $[Fe(CN)_6]^{3-/4-}$ containing 0.1 mol L^{-1} KCl. Inset: the equivalent circuit for obtaining the Nyquit plot in the presence of $[Fe(CN)_6]^{3-/4-}$ probe. (B) The Cottrell plot of current density *vs.* $t^{-1/2}$ of the bare GCE, PCN-222(Fe)/GCE, P3MT/GCE and PMeTh/GCE in 1.0 mmol L^{-1} $[Fe(CN)_6]^{3-/4-}$ containing 10 mmol L^{-1} KCl. (C) CVs at the GCE, PCN-222(Fe)/GCE, P3MT/GCE and PMeTh/GCE in 0.1 mol L^{-1} ABS (pH 4.5) with the presence of 50 μmol L^{-1} L-dopa at the scan rate of 0.1 V s^{-1}. (D) CVs at PMeTh/GCE in 0.1 mol L^{-1} ABS containing 50 μmol L^{-1} L-dopa at various scan rates: 10, 25, 50, 75, 100, 125, 150, 175, 200, 250, 300, 350 mV · s^{-1}. Inset: dependence of redox peak currents on the square root of scan rates. (E) DPVs of 50 μmol L^{-1} L-dopa at PMeTh/GCE in 0.1 mol · L^{-1} ABS with different pH values (3.5, 4.0, 4.5, 4.7, and 5.0). Inset: Dependence of solution pH on the reduction potential. (F) Chronoamperometric response at the PMeTh/GCE in 0.1 mol · L^{-1} ABS with different concentrations of L-dopa: (a) 0, (b) 40, (c) 60, (d) 80 μmol L^{-1}. Inset A: the linear relationship between the peak current (*I*) and $t^{-1/2}$ derived from the chronoamperogram data. Inset B: Dependence of the slope of the straight lines against the L-dopa concentrations.

amount of PMeTh coated on the surface of GCE, the R_{ct} value surprisingly exhibited much lower statistic, to a value of 70 Ω. The remarkable decrease may be ascribed to the inclusion of conductive P3MT (21 Ω) can minimize the barrier for the charge transport and mass transfer impedance at the electrode surface. These results declare that it is possible for the PMeTh/GCE to provide a better platform for the biosensor construction.

The chronoamperometric experiment was also adopted to investigate the effective surface area for the PMeTh/GCE at the interface. According to the Cottrell's equation:

$$I = 2nFAcD^{1/2}\pi^{-1/2}t^{-1/2}$$

where *n* represents the electrons transferred in the redox process (for $[Fe(CN)_6]^{3-/4-}$, n = 1), *c* denotes the concentration of substrate, *D* is

the diffusion coefficient (7.6×10^{-6} cm^2 s^{-1} for $[Fe(CN)_6]^{3-/4-}$), F is Faraday's constant. The effective surface area of the working electrode is denoted by A. As shown in Fig. 5B, the plot of current (I) is proportional to $t^{1/2}$. The slopes for bare, PCN-222(Fe), P3MT, and PMeTh electrodes are 0.0236, 0.0475, 0.0417 and 0.0611 mA s$^{1/2}$ cm^{-2}. As the value of c, D and n are already known, the effective surface area for bare, PCN-222(Fe), P3MT, and PMeTh electrodes was calculated as 0.0786, 0.1582, 0.1389 and 0.2035 cm^2. Obviously, the effective surface area of PMeTh/GCE is about three-folds than that of bare GCE, leading to the additional electrocatalytic sites and a higher sensitivity towards the electrochemical determination.

3.3. Electrochemical detection of L-dopa at PMeTh/GCE

The catalytic performance of L-dopa on each electrode was studied by the cyclic voltammograms (CVs) in the acetate buffer solution (ABS, pH = 4.5). No redox peaks were observed in Fig. S1, implying the PMeTh hybrid material is non-electroactive at the applied potential. As shown in Fig. 5C, all CV curves exhibited a pair of redox peaks after the addition of L-dopa. Improved redox currents at the PCN-222(Fe) (5.268 μA) were observed compared with the naked GCE (3.467 μA), which can be ascribed to the abundant redox active sites in the PCN-222(Fe). The L-dopa molecules can penetrate into the PCN-222(Fe) channels, and the triangular and hexagonal pore structure of PCN-222(Fe) permits the size- and shape-selectivity over the guests that were adsorbed on the electrode surface. More importantly, the noteworthy enlargement peak currents at the P3MT and PMeTh composite electrodes (4.823 and 8.488 μA) were observed as expected. The presence of the P3MT amorphous shell on the surface of the PMeTh composite can increase the current signal and accelerate the charge transfer rate towards L-dopa, which largely depends on its favorable conductivity. In addition, for the PMeTh/GCE, the reduction peak current (I_{pa}) was about 1.1-folds higher than the oxidation peak current (I_{pc}), indicating that the catalytic process towards L-dopa at the PMeTh/GCE was a quasi-reversible process.

3.4. Study of experimental parameters

Different volumes of 3 MT monomer (100, 250, 500, 750, 1000 μL) were also prepared as the same procedure of PMeTh composite. The current reached the maximum when the added volume of 3 MT monomer was 500 μL as shown in Fig. S2. With the volume of 3 MT monomer increased, the electroactive sites of PCN-222(Fe) will be covered, as well as a decrease in surface area. Simultaneously, the P3MT polymerized on the surface of PCN-222(Fe) can serve as a charge collector to increase the electro-conductivity of the PMeTh. When the added volume of 3 MT monomer was 500 μL, the PMeTh composite can fully combine both merits of PCN-222(Fe) and P3MT, leading to the highest current intensity towards L-dopa.

In order to illustrate the electrochemical redox mechanisms, the redox currents (I_p) and the peak potentials (E_p) at different scan rates were investigated and the results were shown in Fig. 5D. As seen in the inset, both the anodic peak current (I_{pa}) and cathodic peak current (I_{pc}) were linear to the square root of scan rates ($\upsilon^{1/2}$). The equations were I_{pa} (μA) = 1.2675 + 0.7709 $\upsilon^{1/2}$ (mV$^{1/2}$ · s$^{-1/2}$) (R^2 = 0.9981); I_{pc} (μA) = −0.6777 − 0.7701 $\upsilon^{1/2}$ (mV$^{1/2}$ · s$^{-1/2}$) (R^2 = 0.9954), indicating the reaction of L-dopa at the PMeTh/GCE is a diffusion controlled process.

The influence of the supporting electrolyte pH value on the electrochemical behavior of the L-dopa was also investigated by differential pulse voltammetry (DPV). As shown in Fig. 5E, the electrochemical response at the PMeTh/GCE is obviously dependent on the pH value. When the DPV trace was recorded under the pH = 4.5 ABS, a maximum and well-defined peak current can be obtained, suggesting the pH = 4.5 is favorable for the L-dopa detection at PMeTh/GCE. Besides, with the pH value increased, the reduction potential moves to a more negative value, indicating the protons have participated in the charge transfer process. The plot in Fig. 5E inset showed that the reduction potentials (E_{pc}) changed linearly with the electrolyte pH value. The equation was E_{pc} (μA) = 0.5807–0.060 pH (R^2 = 0.993). The slope of 60 mV · pH^{-1} was quite equivalent to the theoretical value of 59 mV · pH^{-1} from the Nernst equation, demonstrating the equal number of the protons and electrons transferred in the electrode reaction of L-dopa. As for a quasi-reversible process, the number of electrons transferred in the redox process (n) can be calculated by $\Delta E_p = 2.3RT/\alpha nF$, where α represents the charge transfer coefficient. By assuming the value of α is 0.5, n was calculated to be 1.84, which suggested that there are two electrons transferred in the diffusion process. The total number involved in the L-dopa oxidation was $2H^+$, $2e^-$ mechanism (Prabhu et al., 2011; Hu et al., 2010). The scheme of L-dopa oxidation was shown in Fig. 1B.

From the inset A in Fig. 5F, the peak current (I) was linear to the $t^{-1/2}$. The slopes in inset A also exhibited the linear relationship with the L-dopa concentrations, respectively (inset B of Fig. 5F). According to the Cottrell's equation in the diffusion controlled process, the diffusion coefficient for L-dopa was estimated to 4.33×10^{-5} cm^2 s^{-1}.

3.5. Analytical performance

Under the optimal conditions, the electrochemical determination of L-dopa was further studied by the DPVs technique. Fig. 6A exhibited the DPV traces at the PMeTh/GCE with different concentrations of L-dopa. As exhibited in Fig. 6B, it can be clearly seen that the peak current and

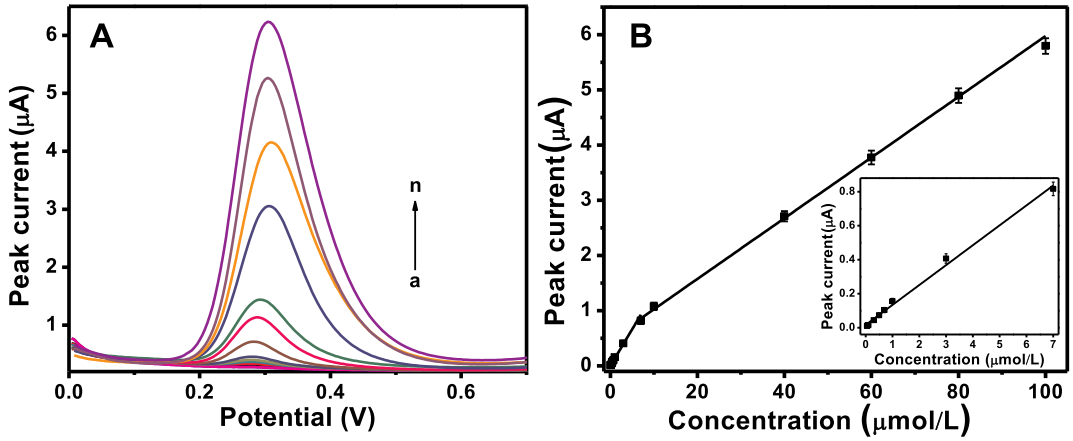

Fig. 6. (A) DPVs at the PMeTh/GCE with various concentrations of L-dopa in the pH 4.5 ABS. (from a to n: 0.05, 0.07, 0.1, 0.3, 0.5, 0.7, 1.0, 3.0, 7.0, 10, 40, 60, 80, 100 μmol L^{-1}). (B) the calibration curve of peak current *vs.* L-dopa concentration. Inset: the tendency of current intensity when L-dopa concentrations are low.

the concentrations of L-dopa possess a good linear relationship within a range of 0.05–100 μmol · L^{-1}. The regression equations over two regions were as follows:

0.05–7.0 μmol · L^{-1}: I_{pa} (μA) = 0.132 C (μmol · L^{-1}) + 0.0036 (R^2 = 0.997)

7.00–100 μmol · L^{-1}: I_{pa} (μA) = 0.055 C (μmol · L^{-1}) + 0.475 (R^2 = 0.998)

The difference in the slopes for the calibration curve at low and high concentrations may be the reasons as follows: At low L-dopa concentrations, small changes in concentrations can cause prominent increment in the current signal which may largely due to the absorption controlled process at the PMeTh/GCE. The small amount of L-dopa is susceptible to form both of thin 2-dimensional (2 D) and thick 3-dimensional (3 D) islands at the redox activities on the modified surface. With the high density of catalytic activities on the surface of the modified electrode (compare with the total numbers of analyte), the L-dopa molecules can be rapidly converted into product at the local concentration of the electrode surface, which contributed to a higher sensitivity in the range of 0.05–7.0 μmol · L^{-1} and the value was calculated as 1.868 μA · μM^{-1} · cm^{-2}. At high L-dopa concentrations, the electrocatalytic sites on the PMeTh composite film were covered up gradually and the mass transport was transferred to the diffusion controlled process. Furthermore, the active sites on the electrode surface was decreased in relation to the total numbers of L-dopa molecules, which may be the main reason for the decrease in the sensitivity to a value of 0.778 μA · μM^{-1} · cm^{-2}.

As seen in Fig. 6A, with the concentration of L-dopa increasing, the oxidation potentials of peak shift to positive potential. The Schottky barrier that formed at the PMeTh/GCE and the L-dopa biomolecule is the main origin of the oxidation potential. The value of potential relies on the electrolyte acidity, scan rate and adsorption of L-dopa biomolecule at different concentrations. After the L-dopa molecules were in large amount, dominant L-dopa molecules will be adsorbed on the electrode surface. The adsorption of L-dopa molecules on the PMeTh/GCE induces a dipole interaction at the interface through the charge transfer, which further modifies the oxidation potential.

The detection limit (LOD) was also estimated as low as 2 nmol L^{-1} (S/N = 3, represented that the concentration of L-dopa is three times the standard deviation about 7 reduplicative detections of the blank solution). The analytical performance of the PMeTh-based sensor was compared with other electrode materials that has been reported recently (Shahrokhian and Asadian, 2009; Hariharan et al., 2011; Arvand and Ghodsi, 2013; Arvand and Ghodsi, 2014; Yue et al., 2017; Sandeep et al., 2018; Silva et al., 2018). As tabulated in Table S1, it is obvious that the fabricated electrode exhibited excellent predominance such as lower detection limit and wider linear region. This superior analytical performance of the PMeTh-based sensor could occur for three reasons: (I) the relative high surface area of PCN-222(Fe) can provide abundant active sites for the oxidation of L-dopa and thus improve the electrochemical response (Feng et al., 2012); (II) the bimetallic metalloporphyrin MOF is constructed by the two metal ions and organic linkers and is capable to interact with the organic molecules through π–π stacking interaction. L-dopa has one aromatic ring. So it is possible for L-dopa to adsorb onto the PCN-222(Fe) through π–π bond between the aromatic ring and the organic linker (Ahmed et al., 2015); (III) the mass transport ability for the PMeTh core-shell composite was dramatically increased via imparting the conductive P3MT polymers (Huang et al., 2017).

3.6. Reproducibility and stability of the L-dopa sensor

The repeatability of the PMeTh electrode was measured by repeating detecting 10 μmol L^{-1} L-dopa (Fig. S3A). After continuous ten run by DPV on one electrode, the relative standard value (R.S.D.) was calculated to be 3.5%, indicating the excellent repeatability of the PMeTh electrode. The reproducibility of this new sensor was also examined by detecting 10 μmol L^{-1} L-dopa at six independent PMeTh/GCE (Fig. S3B), the R.S.D. value was 4.4%, indicating the good fabrication reproducibility in the detection of L-dopa.

The stability is a key parameter for practical applications. The PMeTh-based sensor was exposed to 10 μmol L^{-1} L-dopa in 0.1 mol L^{-1} ABS at a scan rate of 100 mV s^{-1}. It was found that the sensor was relative stable up to 120 cycles without a distinct decrease in its electrocatalytic performance (Fig. S3C). In addition, the electrode was stored at room temperature in a desiccator when not in use. It can retain 90.1% of its initial electrochemical activity towards L-dopa after thirty days (Fig. S3D), demonstrating that this new sensor possessed acceptable long-term stability in the mild condition. On the basis of the reproducibility and stability data, it can be concluded that the core-sell PMeTh composite has an excllent stability, which can be ascribed to the prominent chemical stability both for the PCN-222(Fe) core and P3MT shell.

3.7. Interference study and practical applications

The uric acid (UA) was used to investigate how the similar analyte sturcture might exert influence on the detection of L-dopa. UA is one of the highly electroactive molecules and the oxidation peaks between the UA and L-dopa are almost indistinguishable, making it difficult to further apply in the electochemical sensing applications. As depicted in Fig. S4, it can be clearly seen that there was no obvious current variation for the L-dopa current with injecting UA in pH 4.5 ABS. This result suggested that the PMeTh-based sensor can facilitate the difussion of L-dopa to the electrode surface and give a superior electrocatalytic response in the presence of 10-folds UA. Additionally, other potential interfering substrates were also investigated in this work. The tolerance limit was set as the amount of foregin species causing ± 5% error in the detection of L-dopa. From the tabulation in Table S2, it shows that the proposed modified electrode has an excellent anti-interference. It is likely that the Fe-TCPP of PCN-222(Fe) plays an important role in the selective determination of L-dopa and exclusion of the interferences.

To evaluate the feasibility of the PMeTh-based sensor, the analysis of L-dopa in human urine sample was carried out by standard addition. The human urine samples were collected from the affiliated hospital of Yangzhou University and stored at 0 °C. 1 mL urine sample was diluted with 50 mL 0.1 mol L^{-1} ABS (pH 4.5) to fit the calibration curve and prevent any matrix effect. For real sample analysis, 100 μL sample solution was injected in the 10 mL 0.1 mol L^{-1} ABS (pH 4.5). As shown in Table S3, recoveries of spiked analyte were in the range of 97.0–104.5% with the R.S.D. value were less than 4.4%, indicating the proposed PMeTh/GCE sensor for the reliable and robust detection of L-dopa in real samples is capable.

4. Conclusion

This work presents the successful construction of a novel porph-MOFs based composite electrocatalyst with the P3MT conducting polymer as shell and PCN-222(Fe) as core. The introduction of P3MT effectively promoted the conductivity and improved the charge transport to the electroactive sites provided by PCN-222(Fe). Furthermore, the presence of abundant channels in PCN-222(Fe) can permit the size- and shape-selectivity over the guests. By combination the merits of PCN-222(Fe) and P3MT, we obtained an excellent electrochemical performance towards L-dopa sensing. Moreover, this novel electrochemical sensor exhibited prominent advantages on the wider linear range (0.05–100 μmol L^{-1}), excellent selectivity with reasonable reproducibility and stability. The PMeTh-based sensor was capable to detect L-dopa in the human urine samples with good anti-interference ability. Thus, it is reasonable to anticipate this novel constructed L-dopa

sensor has great potential to apply for clinical diagonesis of L-dopa. We envision that integrating polythiophene derivates into the porph-MOFs has promising perspective for constructing many other excellent biosensors. Currently the preparation of PMeTh composite is tedious, the future work would be in searching for a facile preparation of this kind of core-shell composite.

Acknowledgements

This work was supported by the National Natural Science Foundation of China (21205103, 21275124), Jiangsu Provincial Nature Foundation of China (BK2012258), Young and Middle-aged Academic Leaders Foundation of Yangzhou University, Top-notch Academic Programs Project of Jiangsu Higher Education Institutions (TAPP), and a project funded by the Priority Academic Program Development of Jiangsu Higher Education Institutions (PAPD).

Appendix A. Supplementary data

Supplementary data to this article can be found online at https://doi.org/10.1016/j.bios.2019.111470.

References

Abraira, P.S., Portillo, A.S., Atienzar, P., Bordet, P., Salles, F., Guillou, N., Elkaim, E., Garcia, H., Navalon, S., Horcajada, P., 2019. Dalton Trans. https://doi.org/10.1039/c9dt00917e.
Ahmed, A., Forster, M., Jin, J.S., Myers, P., Zhang, H.F., 2015. ACS Appl. Mater. Interfaces 7, 18054–19063.
Arvand, M., Ghodsi, N., 2013. J. Solid State Electrochem. 17, 775–784.
Arvand, M., Ghodsi, N., 2014. Sensor. Actuator. B Chem. 204, 393–401.
Chen, J.Y., Xu, Q., Shu, Y., Hu, X.Y., 2018. Talanta 184, 136–142.
Damier, P., Hirsch, E.C., Agid, Y., Graybiel, A.M., 1999. Brain 122, 1437–1448.
Feng, D.W., Gu, Z.Y., Li, J.R., Jiang, H.L., Wei, Z.W., Zhou, H.C., 2012. Angew. Chem. Int. Ed. 51, 10307–10310.
Han, P.Y., Liao, J.J., Chang, J.Y., Chang, L.P., Bao, W.R., 2015. RSC Adv. 5, 49343–49349.
Hariharan, V., Radhakrishnan, S., Parthibavarman, M., Dhilipkumar, R., Sekar, C., 2011. Talanta 85, 2166–2174.
Hu, G.Z., Chen, L., Wang, X.L., Shao, S.J., 2010. Electrochim. Acta 55, 4711–4716.
Huang, J.L., Yang, G.J., Meng, W.J., Wu, L.P., Zhu, A.P., Jiao, X.A., 2010. Biosens. Bioelectron. 25, 1204–1211.
Huang, T.Y., Kung, C.W., Liao, Y.T., Kao, S.Y., Cheng, M.S., Chang, T.H., Henzie, J., Alamri, H.R., Alothman, Z.A., Yamauchi, Y., Ho, K.C., Wu, K.C.-W., 2017. Adv. Sci. 4, 1700261.
Kreno, L.E., Leong, K., Farha, O.K., Allendorf, M., Duyne, R.P.V., Hupp, J.T., 2012. Chem. Rew. 112, 1105–1125.
Kung, C.W., Chang, T.H., Chou, L.Y., Hupp, J.T., Farha, O.K., Ho, K.C., 2015. Chem. Commun 51, 2414–2417.
Li, L.Y., Yang, Q.H., Chen, S., Liu, B., Lu, J.L., Jiang, H.L., 2017. Chem. Commun. 53, 10026–10029.
Li, P., Klet, R.C., Moon, S.Y., Wang, T.C., Deria, P., Peters, A.W., Klahr, B.M., Park, H.J., Al-Juaid, S.S., Hupp, J.T., Farha, O.K., 2015. Chem. Commun. 51, 10925–10928.
Liang, Z.B., Qu, C., Xia, D.G., Zou, R.Q., Xu, Q., 2018. Angew. Chem. Int. Ed. 57, 9604–9633.
Liu, W., Zhu, X.Y., 2019. Talanta 197, 59–67.
Ma, Q., Ai, S.Y., Yin, H.S., Chen, Q.P., Tang, T.T., 2010. Electrochim. Acta 55, 6687–6694.
Madani, A., Maouche, N., Riahi, F., Chehimi, M.M., 2015. Ionics 21, 2031–2037.
Prabhu, P., Babu, R.S., Narayanan, S.S., 2011. Sensor. Actuator. B Chem. 156, 606–614.
Sandeep, S., Santhosh, A.S., Swamy, N.K., Suresh, G.S., Melo, J.S., Nithin, K.S., 2018. Mater. Sci. Eng., B 232, 15–21.
Shahrokhian, S., Asadian, E., 2009. J. Electroanal. Chem. 636, 40–46.
Sheng, J.P., Wang, L.Q., Deng, L., Zhang, M., He, H.C., Zeng, K., Tang, F.Y., Liu, Y.N., 2018. ACS Appl. Mater. Interfaces 10, 7191–7200.
Shi, L., Yang, L.Q., Zhang, H.B., Chang, K., Zhao, G.X., Kako, T., 2018. Appl. Catal. B Environ. 224, 60–68.
Silva, T.R., Smaniotto, A., Vieira, I.C., 2018. J. Solid State Electrochem. 22, 1277–1287.
Soumyanath, A., Denne, T., Hiller, A., Ramachandran, S., Shinto, L., 2018. J. Altern. Complement. Med. 24, 182–186.
Sun, D.M., Li, Y.X., Ren, Z.J., Bryce, M.R., Li, H.H., Yan, S.K., 2014. Chem. Sci. 5, 3240–3245.
Thanvi, B.R., Lo, T.C.N., 2004. J. Postgrad. Med. 80, 452–458.
Wang, Y., Chen, H.H., Hu, X.Y., Yu, H., 2016b. Analyst 141, 4647–4653.
Wang, Y., Wang, L., Chen, H.H., Hu, X.Y., Ma, S.Q., 2016a. ACS Appl. Mater. Interfaces 8, 18173–18181.
Wang, Y., Wang, L., Huang, W., Zhang, T., Hu, X.Y., Perman, J.A., Ma, S.Q., 2017. J. Mater. Chem. A 5, 8385–8393.
Wang, Z., Zhang, J.H., Jiang, J.J., Wang, H.P., Wei, Z.W., Zhu, X.J., Pan, M., Su, C.Y., 2018. J. Mater. Chem. A 6, 17698–17705.
Wu, Y.S., Jiang, J.B., Weng, Z., Wang, M.Y., Broere, D.L., Zhong, Y., Brudvig, G.W., Feng, Z.X., Wang, H.L., 2017. ACS Cent. Sci 3, 847–852.
Yue, H.Y., Zhang, H., Huang, S., Lin, X.Y., Gao, X., Chang, J., Yao, L.H., Guo, E.J., 2017. Biosens. Bioelectron. 592–597.
Zhang, L., Chen, G.N., Hu, Q., Fang, Y.Z., 2001. Anal. Chim. Acta 431, 287–292.
Zhang, M.X., Zhou, W., Pham, T., Forrest, K.A., Liu, W.L., He, Y.B., Wu, H., Yildirim, T., Chen, B.L., Space, B., Pan, Y., Zaworotko, M.J., Bai, J.F., 2017. Angew. Chem. Int. Ed. 56, 11426–11430.